ROYAL SOCIETY
OF CHEMISTRY

PAPER

Check for updates

2D self-assembly of *o*-OPE foldamers for chiroptical barcoding†

Irene López-Sicilia,[a] Ana M. Ortuño,*[b] Pablo Reine,[b] Dario Otero,[b] María T. Martín-Romero,[a] Luis Camacho,[a] Luis Álvarez de Cienfuegos, [ID][b] Angel Orte, [ID][c] Juan J. Giner-Casares,*[a] Delia Miguel [ID]*[c] and Juan M. Cuerva [ID]*[b]

We report on the preparation and characterization of two dimensional (2D) films of (*S,S,P*)-**1** and (*R,R,M*)-**1** *ortho*-oligophenylene ethylene (*o*-OPE) enantiomers presenting high values of circularly polarized luminescence (CPL). The amphiphilic character of these two molecules allows a precise 2D self-assembly at the air/water interface and an efficient transfer onto a glass solid support. The morphological and chiroptical characterization of the solid supports after the transfer of 1, 8, 16 and 32 Langmuir films of (*S,S,P*)-**1** and (*R,R,M*)-**1** has been carried out. The strong chiroptical values of these monomers allow reliable ECD measurements to be obtained after a single transfer, with ECD values increasing as the number of transferred films increases. The semi-liquid behavior of the monomers on the solid substrate allows CPL measurements free of photoselection artifacts that show values similar to those obtained in solution and independent of monomer concentration. All these properties have allowed us to develop the first simple organic molecule (SOM)-based chiroptical barcoding presenting positive and negative regions as a proof of concept.

Introduction

Circularly polarized luminescence (CPL) is an attractive property of chiral emissive materials[1–7] because a new degree of freedom can be incorporated into the emitted photons. That is, the sign and even the magnitude of the emission can be used as a new information channel. The unbalanced emission of circularly polarized photons is usually defined by the dimensionless parameter g_{lum}, defined as $g_{lum} = 2(I_L - I_R)/(I_L + I_R)$, also called the luminescence dissymmetry ratio. It can oscillate from ± 2 for pure circular emissions to 0 for unpolarized emissions, thus providing a quantitative estimation of circularly polarized emitted radiation over the total emitted radiation. Despite the numerous potential applications of this property[8–15] we want to focus on information encoding in the solid state. Within this context, the identification of the CPL sign from a luminescent material in different parts of a solid surface could be the base of a chiral barcoding. That is, the uniform fluorescent surface could be only decoded and the information only accessible for suitable receptors. Nevertheless, some potential drawbacks must be taken into account for a successful functioning of the material. First, the material must be emissive in the solid state avoiding the usual problem of the aggregation fluorescence quenching for those materials, while maintaining a reasonable g_{lum} value. Second, non-desirable artifacts derived from photoselection must be avoided. It appears when the detector is perpendicular to the exciting radiation and, at the same time, the emitting entities cannot randomize in space, a usual characteristic of the solid state. It is worth noting that photoselection is a source of linearly polarized light even in the absence of macroscopic anisotropies and that usual CPL-detector architectures can wrongly identify it as circularly polarized light.[2] Third, the solid sample preparation must have a strict control over the amount of emitter present in the material. Although the g_{lum} value is independent of the amount of material, a global intensity not and, in that way, a homogenous emission is guaranteed.

Organic molecules can be deposited on a surface using different techniques (spin coating, drop casting, *etc.*). In this case, Langmuir procedures are especially attractive, allowing for an accurate adjustment of the available area per molecule in a 2D fill at the air/water interface (Fig. 1A).[16] Using this controlled

*[a] Departamento de Química Física y T. Aplicada, Facultad de Ciencias, Universidad de Córdoba, Campus de Rabanales, 14014, Córdoba, Spain.
E-mail: jjginer@uco.es*

[b] Departamento de Química Orgánica, Unidad de Excelencia de Química, C. U. Fuentenueva, Avda. Severo Ochoa s/n E-18071, Universidad de Granada, Spain. E-mail: jmcuerva@ugr.es

[c] Nanoscopy-UGR Laboratory, Departamento de Fisicoquímica, Facultad de Farmacia, Unidad de Excelencia de Química, University of Granada, Granada 18071, Spain. E-mail: dmalvarez@ugr.es

This journal is © The Royal Society of Chemistry 2023

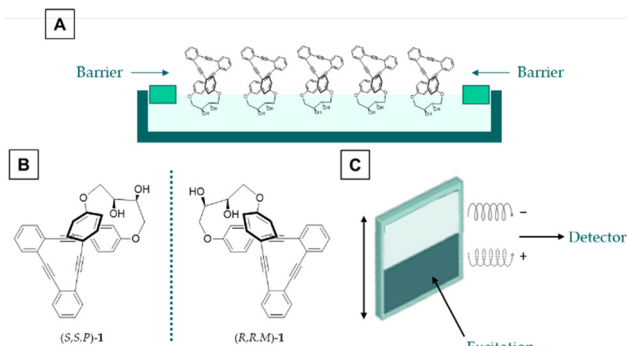*J. Mater. Chem. C*, 2023, **11**, 2591–2599 | **2591**

Fig. 1 Methodology of this work. (a) Langmuir–Schaefer films, (b) employed compounds and (c) CPL based barcoding design.

intermolecular distance, interactions between neighbouring molecules could be tuned and the desired conformation and supramolecular structure might be attained.[17] Therefore, films displaying a well-defined organization at the supramolecular level can be conveniently transferred onto solid substrates.[18,19] Although Langmuir films using chiral molecules are in fact known,[20] the use of enantiopure helical scaffolds is uncommon.[21–27]

As was mentioned above, the use of structures with a high dissymmetric factor is critical. Nevertheless, g_{lum} values are usually in the range of 10^{-3} to 10^{-4} for the majority of the described systems.[28] One of the approximations to enhance g_{lum} is based on the creation of supramolecular entities from monomers with low CPL characteristics.[29–37] It is worth noting that even some of them have been transferred to solid platforms using Langmuir techniques.[38–42] Nevertheless, such supramolecular aggregates or fibers cannot be reoriented after excitation and may be prone to photoselection artifacts if particular architectures are not taken into account.[43,44] Moreover, unexpected dependence of g_{lum} values with the number of transferences has been reported.[42] One potential solution to this drawback is the use of small molecules in which such reorientation/depolarization was efficient even in the solid state. Recently, a continuous effort in designing simple organic molecules (SOMs) with dissymmetric factors in the range of 10^{-2} has resulted in optimized chiral emissive structures.[45] Our group has contributed to this effort developing a family of CPL emitters based on stapled oligo *ortho*-phenylene ethylene (*o*-OPE) architectures with g_{lum} values ranging from 1×10^{-2} to 5×10^{-2}.[46–49] Some of them are especially valuable to form optimal layers in air/liquid interfaces owing to their amphiphilic character, presenting simultaneously hydrophobic and hydrophilic areas.

Herein, we communicate the efficient preparation of Langmuir films (Fig. 1A) of enantiopure diols (*S,S,P*)-**1** and (*R,R,M*)-**1** (Fig. 1B), members of the family of stapled *o*-OPEs, owing to the amphiphilic character of the molecules. They are efficient CPL emitters in the solid state with g_{lum} values comparable to those found in solution. They are also free from photoselection artifacts owing to the quasi-liquid characteristics of the layers in which each individual molecule behaves as in the solution state. Samples with both enantiomers can be prepared and analyzed resulting in a proof of concept of SOM-based CPL barcoding (Fig. 1C). It is worth noting

that usual barcodes are based on positive and null signals. The use of enantiomers allows barcoding based on positive and negative responses, thus increasing the security and reliability of the system.

Results and discussion

Langmuir films

Both enantiomers (*S,S,P*)-**1** and (*R,R,M*)-**1** were prepared as previously described.[47] They were placed on top of a water surface, forming a Langmuir monolayer (Fig. 1A) as demonstrated by the surface pressure–molecular area isotherms in Fig. 2A and Fig. S1 (ESI†). Ultrapure water was used to avoid any effect of ionic strength or pH in the molecular interactions of (*S,S,P*)-**1** and (*R,R,M*)-**1**, thus allowing the corresponding intra- and
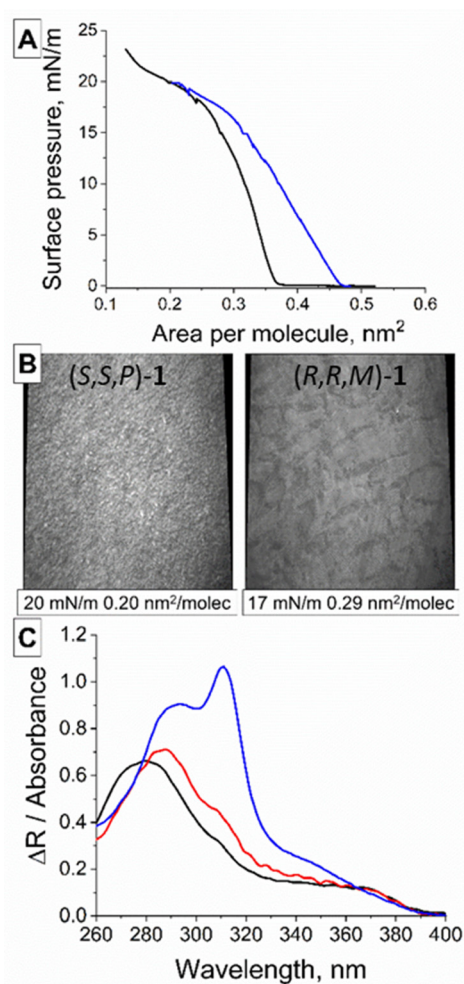

Fig. 2 (A) Surface pressure-molecular area for (*S,S,P*)-**1** (black) and (*R,R,M*)-**1** (blue). (B) Brewster Angle Microscopy pictures of (*S,S,P*)-**1** (left) and (*R,R,M*)-**1** (right) recorded at the air/water interface. The value of the surface pressure and area per molecule is noted in the inset. Width size corresponds to 215 μm. (C) UV-vis reflection and absorbance spectra of (*R,R,M*)-**1**. Black line: Reflection spectrum recorded at 15 mN m^{-1}. Red line: Transmission spectra of one monolayer of (*R,R,M*)-**1** transferred onto a quartz substrate at 15 mN m^{-1}. Blue line: Transmission spectra of bulk solution of (*R,R,M*)-**1**, with dichloromethane as a solvent.

inter-molecular interactions control the resulting supramolecular structure.[50] Although both samples converge to the same isotherm during the collapse of the monolayers (Fig. 2A), some differences were observed at low surface pressure. This abnormal behaviour could be due to diverse and complex contribution of the intermolecular interactions between the molecules forming the monolayer and with the water molecules.[51]

The microscopic morphology of the monolayers could be observed *in situ* at the air/water interface using Brewster Angle Microscopy (BAM), see Fig. 2B and Fig. S2, S3 (ESI†).[52] The BAM pictures of (*S*,*S*,*P*)-**1** and (*R*,*R*,*M*)-**1** at the early stages of compression revealed a fibrillar texture and a homogenous film, respectively. Both films of (*S*,*S*,*P*)-**1** and (*R*,*R*,*M*)-**1** evolved onto a solid monolayer when increasing the surface pressure showing a compact structure with bright granules.

In situ UV-vis reflection spectroscopy was used to attain molecular details on the arrangement of (*R*,*R*,*M*)-**1** at the air/water interface (Fig. 2C).[53] Computer simulations under *in vacuo* conditions predicted five UV-vis bands at 356.9, 317.1, 311.3, 293.5 and 284.1 nm (Fig. S4, ESI†). The experimentally observed UV-vis bands were consistent with those obtained by computer simulations. The different bands are related to transition dipoles that display different orientations (Fig. S5, ESI†). Therefore, the UV-vis spectra at air/water and air/solid interfaces provide information about the relative orientation of the (*R*,*R*,*M*)-**1** molecules. The UV-vis reflection spectrum recorded at the air/water interface displayed a main band centred at *ca.* 284 nm and a broad shoulder at 355 nm, with comparatively reduced contributions from the bands at 317, 311 and 293 nm. This UV-vis spectrum corresponds to an almost upright arrangement of the (*R*,*R*,*M*)-**1** molecules at the air/water interface (Fig. S5, ESI†).

By comparing the UV-vis reflection spectra of (*R*,*R*,*M*)-**1** monolayers recorded at the air/water interface with the UV-vis transmission spectra recorded at a solid substrate with the transferred monolayers, the modification of the supramolecular arrangement upon transference can be assessed.[54] The UV-vis spectra were found to overlap almost entirely for both spectra, thus indicating the small modification in the supramolecular arrangement of (*R*,*R*,*M*)-**1** molecules when transferred from the air/water interface to a solid support (Fig. 2C and Fig. S4, ESI†).

On the other hand, the UV-vis transmission spectrum recorded from a bulk solution of (*R*,*R*,*M*)-**1** in dichloromethane displayed a significantly different shape, with the mentioned five absorption bands as expected from a non-preferred orientation corresponding to (*R*,*R*,*M*)-**1** molecules in solution.[55] Remarkably, the band centred at *ca.* 317 nm showed the highest intensity for the bulk solution but appeared as a small shoulder for the UV-vis spectra recorded at interfaces, thus confirming the relevance of the orientation of the (*R*,*R*,*M*)-**1** molecules when analysing the UV-vis spectra (Fig. S6–S8, ESI†).

Computer simulations using molecular dynamics methods further confirmed the proposed supramolecular arrangement (Fig. 3). Monolayers of either (*S*,*S*,*P*)-**1** or (*R*,*R*,*M*)-**1** were built on a water surface, reaching an equilibrium state in which the tilting angle values of the main axis of the molecules with respect to the *Z* axis was 17.2° and 14.5° for (*S*,*S*,*P*)-**1** and
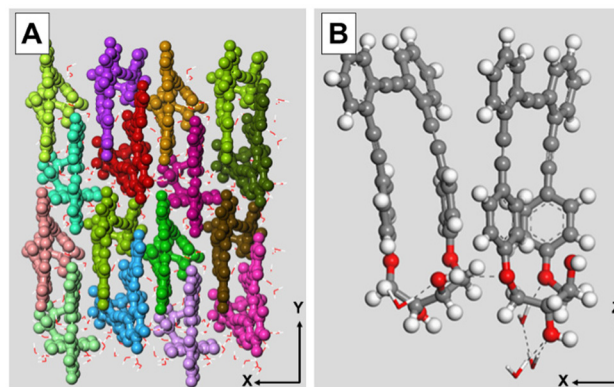

Fig. 3 (A) Top view of a monolayer of (*R*,*R*,*M*)-**1** molecules onto a water surface. XYZ dimension values of the computational box were 24 × 30 × 150 Å³. Water molecules are depicted as sticks for clarity. (B) Close detail of (*R*,*R*,*M*)-**1** molecules in the monolayer. Additional (*R*,*R*,*M*)-**1** and water molecules are omitted for clarity. The formation of intermolecular H-bonds between neighbour (*R*,*R*,*M*)-**1** molecules and H-bonds with water is displayed as a dashed black line, left and right, respectively.

(*R*,*R*,*M*)-**1**, respectively. This computational result is in agreement with the enantiomeric character of the two molecules within the subtle errors derived from molecular mechanics. The main feature is that this reduced value of tilting is consistent with an almost upright arrangement of the molecules on the air/water and air/solid interfaces and therefore with the UV-vis results described above. The number of hydrogen-bonds (H-bonds) could be obtained as well, see Table S2 (ESI†). H-bonds play an important role in sustaining the supramolecular architecture, showing as expected negligible differences of number of formed H-bonds between (*S*,*S*,*P*)-**1** and (*R*,*R*,*M*)-**1**.

AFM characterization

Langmuir films transferred onto glass slides were further analysed by atomic force microscopy (AFM) to give insights into the behaviour of multiple transference process on the topology of the material. AFM topographical measurements showed the particular arrangement of compound (*S*,*S*,*P*)-**1** over the glass slide. As can been seen from Fig. 4, multiple transferences of Langmuir films onto the glass did not generate a continuous and uniform film of the compound; rather it led to the formation of relatively homogeneous nanometer-sized aggregates that grew in height and width as the number of layers transferred to the glass increased. This phase separation to generate individual aggregates once transferred on solid supports is well documented for polymer blends in which the process depends on several factors such as, type of solvent, chemical structure and evaporation rate.[56] It has also been studied for amphiphilic semifluorinated alkanes and surge by the packing strain of molecules containing different steric volume regions, thick fluorinated chains *versus* thin hydrogenated chains.[57,58] Similarly, compound (*S*,*S*,*P*)-**1** also has two very distinct regions, the aromatic and the hydroxyls, which differ significantly in polarity and steric volume. Fig. 4A shows the 3D topography of a glass slide after the transference of 8 Langmuir films in which
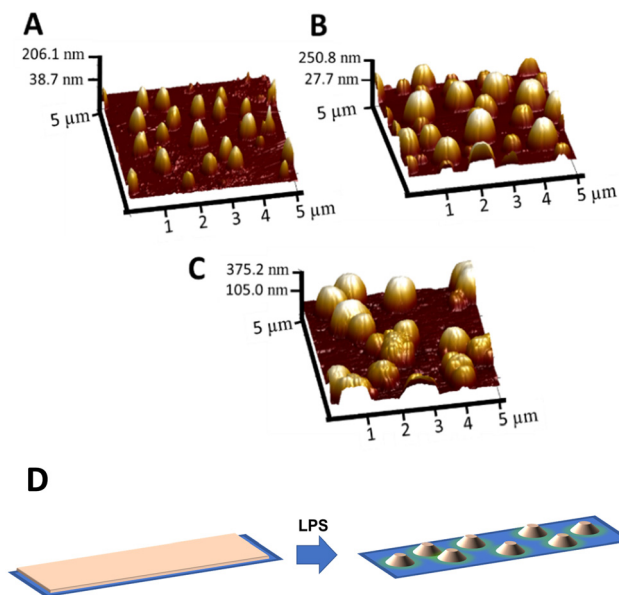
This journal is © The Royal Society of Chemistry 2023

J. Mater. Chem. C, 2023, **11**, 2591–2599 | **2593**

Fig. 4 AFM images, topography in 3D (5 μm × 5 μm), of Langmuir films of compound (S,S,P)-**1** transferred onto glass slides after subsequent deposition of 8 layers (A), 16 layers (B) and 32 layers (C). Proposed mechanism of liquid phase separation causing the morphology of the films (D).

the average maximum height is 72.4 nm. This height that is the result of compound (S,S,P)-**1** accumulation, increases as the number of Langmuir films transferred onto the glass increases. The transference of 16 films (Fig. 4B) shows an average maximum height of 117 nm and the transference of 32 films (Fig. 4C) shows an average maximum height of 207 nm. The accumulation of compound (S,S,P)-**1** within a confined nanometer size area is essential for the desired chiroptical properties since these aggregates lie in a separated fluid liquid phase and therefore can reorient after excitation avoiding photoselection artefacts. Moreover, the possibility of controlling the density of compound per area using iterative film deposition in a controlled and reproducible way allows modulating the global intensity of emission introducing another tuneable parameter to encode information.

Optical characterization

The UV-vis spectra of the transferred films are in agreement with the previously reported one in solution with maxima at 293 and 310 nm, also in agreement with the liquid phase separation. As expected global absorbance of the sample increases linearly with the number of transferences (Fig. 6A).

Fluorescence spectra of (S,S,P)-**1** or (R,R,M)-**1** transferred to glass supports are also in agreement with those previously reported,[46] exhibiting an emission band centred at 414 nm (Fig. S15 and S16, ESI†). However, the fluorescence intensity does not scale linearly with the amount of sample deposited, which is consistent with the presence of aggregation-induced quenching. Hence, to avoid further quenching, the global emission was optimized with a maximum of 32 transferences.

The transferred films of compounds (S,S,P)-**1** or (R,R,M)-**1** were also analysed by fluorescence lifetime imaging microscopy (FLIM), which provides contrast from both the emission
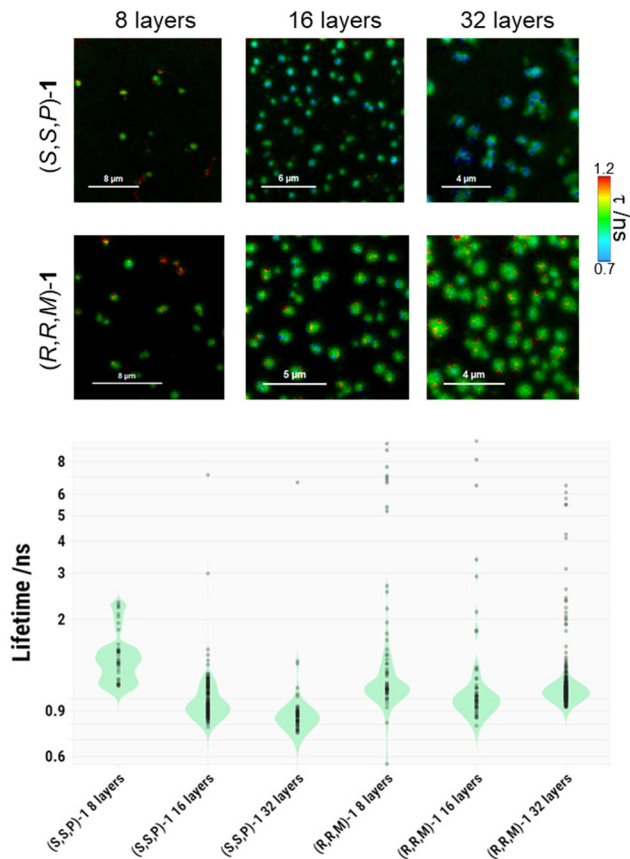

Fig. 5 Representative FLIM images of compounds (S,S,P)-**1** and (R,R,M)-**1** transferred onto glass slides after subsequent deposition of 8, 16, or 32 layers; and the corresponding violin plot of the particle-wise analysis from, at least, 3 different images in each case.

intensity and the kinetics of the excited-state *via* the fluorescence lifetime, τ, values. Fig. 5 and Fig. S9 (ESI†) show that FLIM images were in good agreement with AFM experiments, so that the transferred layers of compounds (S,S,P)-**1** or (R,R,M)-**1** resulted in a clear phase separation, where the emissive molecules accumulated. These regions were segmented and, using a particle-wise analysis, the population of different lifetimes were obtained (Fig. 5). For both compounds, increasing the number of transferred layers caused a decrease in the average τ values. Nevertheless, several regions that exhibited long τ values were occasionally detected, especially in (R,R,M)-**1**, indicating certain degree of heterogeneity, as can be seen in the violin plot in Fig. 5. In such cases, it is useful to compare the median values for the different populations, that were 1.50 ns for 8 layers, 0.94 ns for 16 layers and 0.86 ns for 32 layers in (S,S,P)-**1**; and 1.14 ns for 8 layers, 1.01 ns for 16 layers and 1.06 ns for 32 layers in (R,R,M)-**1**. Fluorescence lifetimes of both enantiomers were also analyzed in CH_2Cl_2 solutions. In this case, the average lifetime of (S,S,P)-**1** was 4.84 ns whereas for (R,R,M)-**1** presents a similar value of 4.59 ns. Some populations with these longer lifetimes can be also detected in minor quantities for both compounds in the transferred systems. The decrease in τ upon the transfer and further increasing the number of transferred layers is consistent with a self-quenching process due to aggregation in the separated phase.

2594 | *J. Mater. Chem. C*, 2023, **11**, 2591–2599

This journal is © The Royal Society of Chemistry 2023

Chiroptical characterization

For our purpose, the chiroptical response of diols (S,S,P)-**1** and (R,R,M)-**1** in the solid state should be as intense as in solution to obtain clear and reliable signals. Nevertheless, cautions about the influence of macroscopic anisotropies in the signal must be also taken into account. The invariance of the signal after a flipping process guarantees the inexistence of a synergic contribution of linear dichroism (LD) and linear birefringence (LB) to the global signal (Fig. S22, ESI†).[14] Nevertheless, LD spectra showed weak but not null signal at relevant wavelengths (Fig. S21, ESI†). In such situations the intrinsic signal of the sample must be obtained as an average value of different acquisitions obtained by rotation of the sample around the optical axis (Scheme S2, ESI†). In our case, we selected eight different orientations.

As far as the reliability of the electronic circular dichroism (ECD) signal is concerned the study of samples with different number of transferences (from 1 to 32) showed two key findings: (i) the response is similar in shape and g_{abs} values to those obtained in diluted solutions (Fig. 6B and Table S3, ESI†), and (ii) the intensities of ECD spectra in terms of differential absorbance (ΔA) is directly proportional to the amount of matter deposited (Fig. 6B). Regarding to this latter property a simple normalization showed that each transference process contribute equally $(\Delta A = 1.4 \times 10^{-2}\ mA)$ to the total differential absorbance with a global g_{abs} value of 2.2×10^{-3} at 371 nm (Fig. S18A, ESI†). Accordingly with that value a reliable ECD

signal can be also obtained with only one transference, showing that the chiroptical response in this case is able to be detected from a single molecular layer (Fig. S18B, ESI†). This result is highly infrequent, pointing out the versatility of diol **1**.[24,59]

CPL measurements of solid samples are usually more delicate due to the fact that they can be heavily affected by LD of the sample and photoselection. Uncertainties derived from LD can be alleviated owing to the cosine dependence with respect to the rotation of the sample, as in the case of ECD. Nevertheless, removing photoselection artefacts requires the depolarization process of diol **1** in the solid state. It is worth noting that the analysis of fluorescence anisotropy in the samples can shed light on the presence of interferences due to photoselection and/or the formation of ordered, liquid crystal-like phases. For that purpose the multi-layers of (S,S,P)-**1** or (R,R,M)-**1** transferred onto glass slides were analysed using different settings for the 375 nm excitation light: 0° and 90° linearly polarized light and right (R-CPL) and left circularly polarized light (L-CPL). The collected emission from the specimen was separated into the vertical (I_V) and the horizontal (I_H) polarization components. We then reconstructed images for the I_H/I_V ratio and obtained population histograms after thresholding to remove background pixels.

In Fig. 7 we show an example of the images of one sample (7A) and the histograms obtained for the sum of all the samples (7B) with 16 monolayers of diol (S,S,P)-**1** using the four types of excitation and the corresponding extracted populations. As it can be seen, very similar distributions were obtained in all cases, with slight differences between linear excitations but
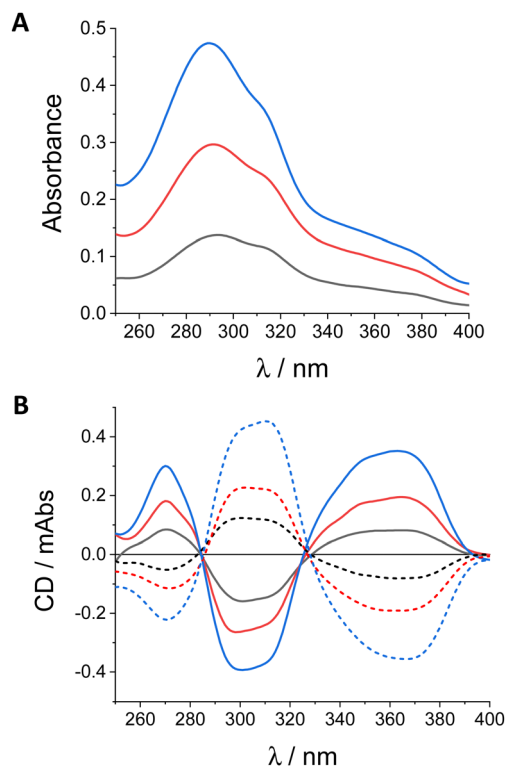

Fig. 6 (A) Absorbance and (B) CD spectra of (S,S,P)-**1** (continuous lines) and (R,R,M)-**1** (discontinuous lines) in quartz plates with 8 (black line), 16 (red line) and 32 (blue line) layers.
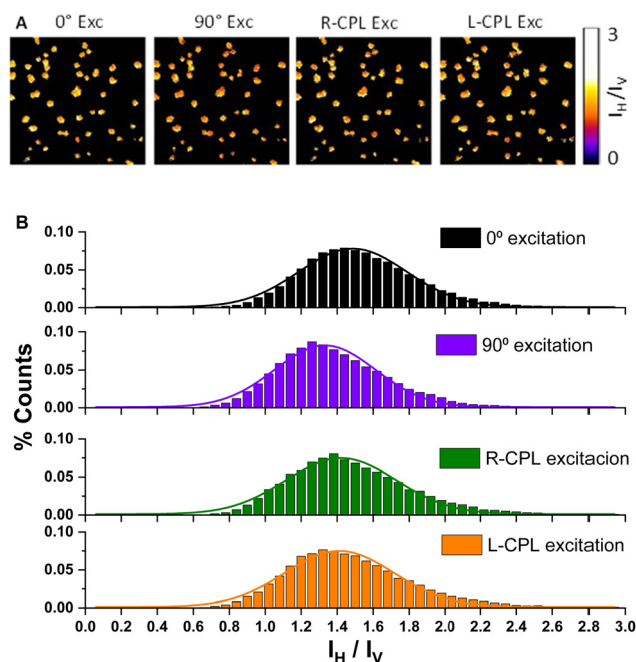
Fig. 7 (A) Examples of different I_H/I_V ratio images and (B) extracted overall I_H/I_V ratio histograms (from, at least, 4 different images) of compound (S,S,P)-**1** transferred onto glass slides after subsequent deposition of 16 layers at different excitation polarizations.

This journal is © The Royal Society of Chemistry 2023

J. Mater. Chem. C, 2023, **11**, 2591–2599 | **2595**

Fig. 8 (A) Method used for measuring CPL values of compounds transferred onto glass slides. (B) g_{lum} and C) ΔI values of (S,S,P)-**1** (continuous lines) and (R,R,M)-**1** (discontinuous lines) in quartz plates with 8 (black line), 16 (red line) and 32 (blue line) layers. Excitation wavelength: 250 nm.
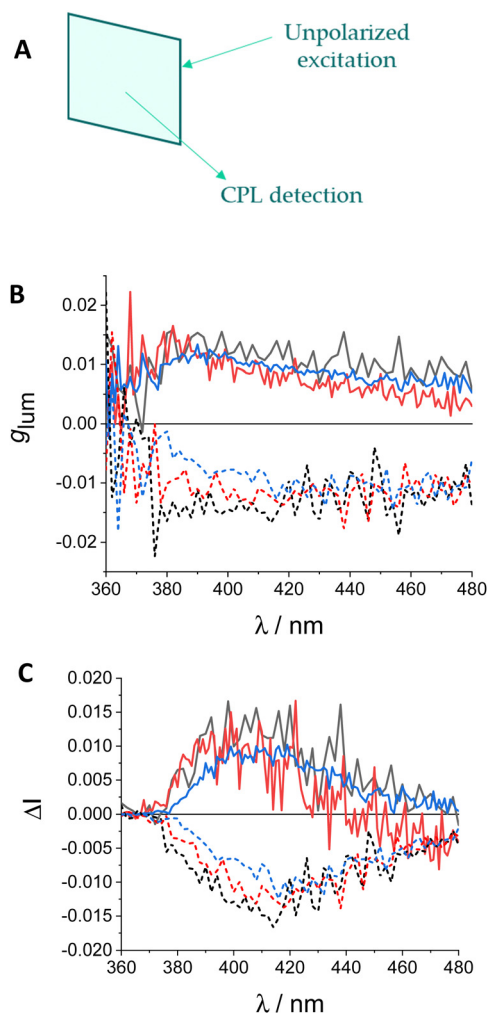

Fig. 9 (A) CD values of 1 (green inverted trianles), 8 (dark blue triangles), 16 (red circles) and 32 (black squares) layers of (S,S,P)-**1**, and 1 (purple diamonds), 8 (yellow triangles), 16 (light blue triangles) and 32 (gray circles) layers of (R,R,M)-**1**. (B) Integral of g_{lum} graph of (S,S,P)-**1** (green areas) and (R,R,M)-**1** (purple areas) layers in the selected wavelength region (410–430 nm). See Fig. S25 and S26 (ESI†) for raw data.

almost identical curves for different senses of CPL, thus supporting the absence of microscopic anisotropy in these samples. These results are reproducible independently of the number of transferences and for both enantiomers (see Fig. S10–S14, ESI†). Overall, the isotropic emission of both enantiomers upon different types of excitation confirmed that artefacts from photoselection can be neglected when measuring CPL emission.

Once this latter source of artifacts has been ruled out by taking into account the depolarization process of diol **1**, free-of-artefact CPL signal could be obtained for compounds (S,S,P)-**1** and (R,R,M)-**1** in layers transferred onto quartz slides with a g_{lum} value of 1.2×10^{-2} (Fig. 8). This value is independent of the number of transferences and matches the one obtained in diluted solutions, pointing out a true molecular origin of the emission.

Chiral barcoding

With the confidence of having reliable values for ECD and CPL for enantiomers (S,S,P)-**1** and (R,R,M)-**1** in layers transferred we decided to generate a simple chiral barcoding presenting
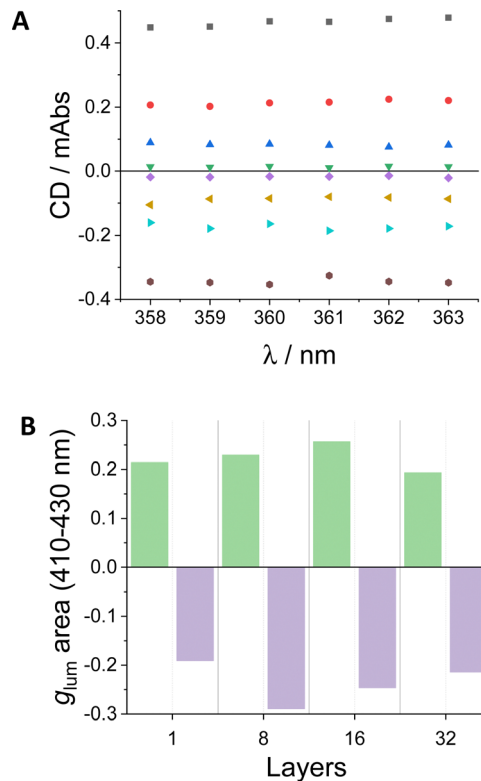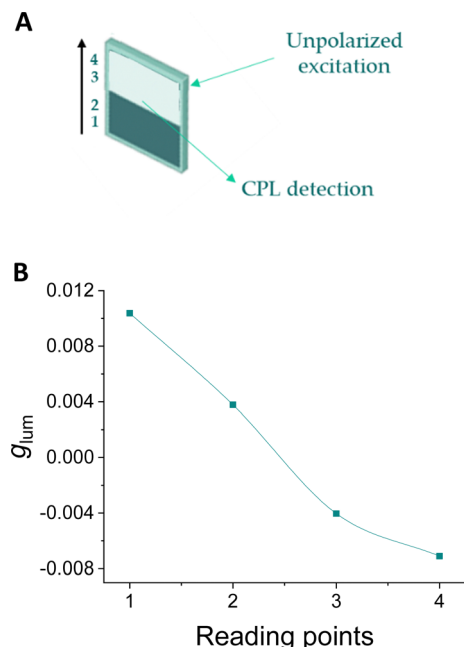
alternating positive and negative regions. For that, we built two different barcodes, one with 16 and the second with 32 layers, by mixing substrates with the same number of transferences of each of the enantiomers. So we prepared the enantiomerically pure samples and the two different regions were created by cutting and pasting quartz with deposited (S,S,P)-**1** and (R,R,M)-**1**.

Within this context, recording the complete ECD or CPL spectra is not strictly required. The detection in a small wavelength range around the maxima (ECD, 358–363 nm, CPL, 410–430 nm) would be enough. Such conditions were explored for the prepared samples using from 1 to 32 transferences of either (S,S,P)-**1** and (R,R,M)-**1** (Fig. 9). Owing to the intense chiroptical response of the enantiomers of diol **1**, the samples gave a stable value in sign and magnitude for all the specimens including from 1 to 32 transferences with only 8 accumulations, each in one different rotation with a global acquisition time of around 10 s (CD) and 20 s (CPL). For the case of CPL we found that it is also informative the relative integral of the g_{lum} spectra integrated over the measured region. In that case point by point deviations derived for the short acquisition times can be averaged and compared between the different experiences (Fig. 9). Highly homogeneous signals can be therefore observed.

Finally, the case of 32 transferences was selected as optimal in terms of signal/noise ratio, time and amount of material to

2596 | J. Mater. Chem. C, 2023, **11**, 2591–2599

This journal is © The Royal Society of Chemistry 2023

Fig. 10 (A) Method used for reading barcodes at 4 points, from (S,S,P)-**1** to (R,R,M)-**1**. (B) Reading of a barcode with two bands of 32 layers of (S,S,P)-**1** to (R,R,M)-**1**. Average signal of a small wavelength range. See Fig. S28 (ESI†) for raw data.

check the response in the chiral barcoding. The tracking of the signal in a dual barcoding is shown in Fig. 10. The excitation focus was manually displaced along the indicated axis. In the extrema only one enantiomer is irradiated. At the inner points the g_{lum} value diminished slightly owing to excitation is also covering a small part of the other enantiomer region. A clear sigmoidal curve can be observed as expected along the tracking process for each wavelength and the corresponding average.

Conclusions

In summary, we have shown that enantiomeric (S,S,P)-**1** and (R,R,M)-**1** o-OPEs are able to efficiently self-assemble in 2D films thanks to their amphiphilic nature. The transference of these films in glass supports has allowed the study and chiroptical evaluation of solid materials cover exclusively with SOMs. Films deposited on these substrates suffer a process of phase separation giving rise to discrete aggregates that increase in size as the number of transferred films increases. This effect not only does not affect chiroptical values, but it is also a great advantage since the monomers in these aggregates can be reoriented avoiding photoselection processes. This result is essential to develop reliable systems and is difficult to obtain using other types of compounds, like supramolecular polymers, and/or deposition processes. State-of-the-art spectroscopic techniques have been used to prove that the emission values of the substrates are free of artefacts. With this verification and coupled with the high emission values of the monomers that are preserved in the solid substrates we have been able to develop a CPL-barcoding system as a proof of concept. The possibility of using both

enantiomers makes it possible to develop a barcoding system that can present positive and negative regions or values, making it easier and safer to read.

Although the results presented here are a proof of concept, the significant progress in recent years of molecules and systems showing high CLP values and techniques or instruments capable of measuring it suggests that this property will soon be exploited in commercialized products.

Author contributions

Conceptualization: J. J. G. C., D. M., J. M. C.; data curation: A. M. O., I. L. S., M. T. M. R., L. C., L. A. C., A. O., J. J. G. C., D. M.; formal analysis: A. M. O., I. L. S., M. T. M. R., L. A. C., A. O., J. J. G. C., D. M., J. M. C.; funding acquisition: J. J. G. C., D. M., J. M. C.; investigation: A. M. O., I. L. S., P. R., D. O., M. T. M. R., L. C., L. A. C., A. O., J. J. G. C., D. M., J. M. C,; methodology: L. C., A. O., J. J. G. C., D. M.; project administration: J. J. G. C., D. M., J. M. C.; resources: J. J. G. C., D. M., J. M. C.; software: L. C., A. O., D. M.; supervision: J. J. G. C., D. M., J. M. C.; validation: J. J. G. C., D. M., J. M. C.; visualization: A. M. O., I. L. S., M. T. M. R., L. C., L. A. C., A. O., J. J. G. C., D. M.; writing – original draft: J. J. G. C., J. M. C., A. M. O., L. A. C., A. O., D. M.; writing – review & editing: all authors.

Conflicts of interest

There are no conflicts to declare.

Acknowledgements

Notes and references

1 J. P. Riehl and F. S. Richardson, Circularly Polarized Luminescence Spectroscopy, *Chem. Rev.*, 1986, **86**, 1–16.

2 G. Longhi, E. Castiglioni, J. Koshoubu, G. Mazzeo and S. Abbate, Circularly Polarized Luminescence: A Review of Experimental and Theoretical Aspects, *Chirality*, 2016, **28**, 696–707.

3 T. Mori, *Circularly Polarized Luminescence of Isolated Small Organic Molecules*, Springer Nature Singapore Pte Ltd, Singapore, 1st edn, 2020, pp. 1–338, DOI: **10.1007/978-981-15-2309-0**.

This journal is © The Royal Society of Chemistry 2023

J. Mater. Chem. C, 2023, **11**, 2591–2599 | **2597**

4 H.-Y. Wong, W.-S. Lo, K.-H. Yim and G.-L. Law, Chirality and Chiroptics of Lanthanide Molecular and Supramolecular Assemblies, *Chem*, 2019, **5**, 3058–3095.

5 B. Doistau, J.-R. Jiménez and C. Piguet, Beyond Chiral Organic (P-Block) Chromophores for Circularly Polarized Luminescence: The Success of D-Block and F-Block Chiral Complexes, *Front. Chem.*, 2020, **8**, 555.

6 Y. Sang, J. Han, T. Zhao, P. Duan and M. Liu, Circularly Polarized Luminescence in Nanoassemblies: Generation, Amplification, and Application, *Adv. Mater.*, 2020, **32**, 1900110.

7 A. H. G. David and J. F. Stoddart, Chiroptical Properties of Mechanically Interlocked Molecules, *Isr. J. Chem.*, 2021, **61**, 608–621.

8 C. Wang, L. Liu, J. Wang and Y. Yan, Electrochemically Switchable Circularly Polarized Photoluminescence within Self-Assembled Conducting Polymer Helical Microfibers, *J. Am. Chem. Soc.*, 2022, **144**, 19714–19718.

9 D. Parker, J. D. Fradgley and K.-L. Wong, The Design of Responsive Luminescent Lanthanide Probes and Sensors, *Chem. Soc. Rev.*, 2021, **50**, 8193–8213.

10 D.-W. Zhang, M. Li and C.-F. Chen, Recent Advances in Circularly Polarized Electroluminescence Based on Organic Light-Emitting Diodes, *Chem. Soc. Rev.*, 2020, **49**, 1331–1343.

11 J. Jiménez, L. Cerdán, F. Moreno, B. L. Maroto, I. García-Moreno, J. L. Lunkley, G. Muller and S. de la Moya, Chiral Organic Dyes Endowed with Circularly Polarized Laser Emission, *J. Phys. Chem. C*, 2017, **121**, 5287–5292.

12 L. E. MacKenzie and R. Pal, Circularly Polarized Lanthanide Luminescence for Advanced Security Inks, *Nat. Rev. Chem.*, 2021, **5**, 109–124.

13 S. C. J. Meskers, Circular Polarization of Luminescence as a Tool To Study Molecular Dynamical Processes, *ChemPhotoChem*, 2022, **6**, e202100154.

14 G. Albano, G. Pescitelli and L. Di Bari, Chiroptical Properties in Thin Films of π-Conjugated Systems, *Chem. Rev.*, 2020, **120**(18), 10145–10243.

15 M. Li and C.-F. Chen, Advances in circularly polarized electroluminescence based on chiral TADF-active materials, *Org. Chem. Front.*, 2022, **9**, 6441.

16 J. J. Giner-Casares, G. Brezesinski and H. Möhwald, *Curr. Opin. Colloid Interface Sci.*, 2014, **19**, 176–182.

17 P. Mondal, G. Manna, T. Kamilya, M. Das, K. Ariga, G. J. Richards, J. P. Hill and S. Acharya, *Adv. Mater. Interfaces*, 2022, **9**, 2200209.

18 K. Ariga, *Langmuir*, 2020, **36**, 7158–7180.

19 G. Giancane, S. Bettini, L. Valli, V. Bracamonte, M. Carraro, M. Bonchio and M. Prato, *J. Mater. Chem. C*, 2021, **9**, 16290–16297.

20 N. Nandi and D. Vollhardt, Chiral discrimination and recognition in Langmuir monolayers, *Curr. Opin. Colloid Interface Sci.*, 2008, **13**, 40–46.

21 F. Feng, T. Miyashita, H. Okubo and M. Yamaguchi, Spreading Behavior of Optically Active Macrocycloamides Consisting of Helical Chiral Units at the Air–Water Interface and the Formation of Langmuir–Blodgett Films, *J. Am. Chem. Soc.*, 1998, **120**, 10166–10170.

22 M. Gon, R. Sawada, Y. Morisaki and Y. Chujo, Enhancement and Controlling the Signal of Circularly Polarized Luminescence Based on a Planar Chiral Tetrasubstituted [2.2]Paracyclophane Framework in Aggregation System, *Macromolecules*, 2017, **50**, 1790–1802.

23 T. Verbiest, S. Van Elshocht, M. Kauranen, L. Hellemans, J. Snauwaert, C. Nuckolls, T. J. Katz and A. Persoons, Strong Enhancement of Nonlinear Optical Properties Through Supramolecular Chirality, *Science*, 1998, **282**, 913–915.

24 C. Nuckolls, T. J. Katz, T. Verbiest, S. V. Elshotch, H.-G. Kuball, S. Kieswalter, A. J. Lovinger and A. Persoons, Circular Dichroism and UV–Visible Absorption Spectra of the Langmuir–Blodgett Films of an Aggregating Helicene, *J. Am. Chem. Soc.*, 1998, **120**, 8656–8660.

25 H. Okubo, F. Feng, D. Nakano, T. Hirata, M. Yamaguchi and T. Miyashita, Synthesis and monolayer behaviors of optically active 1,12-dimethylbenzo[c]phenanthrene-5,8-diamides and the formation of chiral Langmuir–Blodgett films, *Tetrahedron*, 1999, **55**, 14855–14864.

26 N. Kayes, M. Shahabuddin, J. Miah, M. Karikomi, S. Yoshihara, E. Nasuno, N. Kato and K. I. Iimura, Thin films of an axially chiral bibenzo[c]phenanthrene diol and its enantiomers: Film structure, optical property, and photoelectrochemical response, *Colloids Surf., A*, 2018, **538**, 155–163.

27 J. Holec, J. Rybacek, J. Vacek, M. Karras, L. Bednarova, M. Budesinsky, M. Slusna, P. Holy, B. Schmidt, I. G. Stara and I. Stary, Chirality-Controlled Self-Assembly of Amphiphilic Dibenzo[6]helicenes into Langmuir–Blodgett Thin Films, *Chem. – Eur. J.*, 2019, **25**, 11494–11502.

28 H. Tanaka, Y. Inoue and T. Mori, Circularly Polarized Luminescence and Circular Dichroisms in Small Organic Molecules: Correlation between Excitation and Emission Dissymmetry Factors, *ChemPhotoChem*, 2018, **2**, 386–402.

29 J. Kumar, T. Nakashima, H. Tsumatori, M. Moti, M. Naito and T. Kawai, Circularly Polarized Luminescence in Supramolecular Assemblies of Chiral Bichromophoric Perylene Bisimides, *Chem. – Eur. J.*, 2013, **19**, 14090–14097.

30 J. Kumar, T. Nakashima, H. Tsumatori and T. Kawai, Circularly Polarized Luminescence in Chiral Aggregates: Dependence of Morphology on Luminescence Dissymmetry, *J. Phys. Chem. Lett.*, 2014, **5**, 316–321.

31 H. Li, J. Cheng, Y. Zhao, J. W. Lam, H. S. Wong, H. Wu, B. Li and B. Z. Tang, l-Valine methyl ester-containing tetraphenylethene: aggregation-induced emission, aggregation-induced circular dichroism, circularly polarized luminescence, and helical self-assembly, *Mater. Horiz.*, 2014, **1**, 518–521.

32 H. Li, J. Cheng, H. Deng, E. Zhao, B. Shen, J. W. Y. Lam, K. S. Wong, H. Wu, B. S. Li and B. Z. Tang, Aggregation-induced chirality, circularly polarized luminescence, and helical self-assembly of a leucine-containing AIE luminogen, *J. Mater. Chem. C*, 2015, **3**, 2399–2404.

33 Q. Ye, D. Zhu, H. Xu, X. Lu and Q. Lu, The fabrication of helical fibers with circularly polarized luminescence via ionic linkage of binaphthol and tetraphenylethylene derivatives, *J. Mater. Chem. C*, 2016, **4**, 1497–1503.

34 F. Salerno, J. A. Berrocal, A. T. Haedler, F. Zinna, E. W. Meijer and L. Di, Bari, Highly circularly polarized broad-band

2598 | *J. Mater. Chem. C*, 2023, **11**, 2591–2599

This journal is © The Royal Society of Chemistry 2023

emission from chiral naphthalene diimide-based supramolecular aggregates, *J. Mater. Chem. C*, 2017, **5**, 3609–3615.

35 F. Song, Z. Xu, Q. Zhang, Z. Zhao, H. Zhang, W. Zhao, Z. Qiu, C. Qi, H. Zhang, H. H. Y. Sung, I. D. Williams, J. W. Y. Lam, Z. Zhao, A. Qin, D. Ma and B. Z. Tang, Highly Efficient Circularly Polarized Electroluminescence from Aggregation-Induced Emission Luminogens with Amplified Chirality and Delayed Fluorescence, *Adv. Funct. Mater.*, 2018, **28**, 1800051.

36 Z. Zong, P. Zhang, H. Qiao, A. Hao and P. Xing, Chiral toroids and tendril superstructures from integrated ternary species with consecutively tunable supramolecular chirality and circularly polarized luminescence, *J. Mater. Chem. C*, 2020, **8**, 16224–16233.

37 S. Hu, L. Hu, X. Zhu, Y. Wang and M. Liu, Chiral V-shaped Pyrenes: Hexagonal Packing, Superhelix, and Amplified Chiroptical Performance, *Angew. Chem., Int. Ed.*, 2021, **60**, 19451–19457.

38 J. A. Kitchen, D. E. Barry, L. Mercs, M. Albrecht, R. D. Peacock and T. Gunnlaugsson, Circularly Polarized Lanthanide Luminescence from Langmuir–Blodgett Films Formed from Optically Active and Amphiphilic EuIII-Based Self-Assembly Complexes, *Angew. Chem., Int. Ed.*, 2012, **51**, 704–708.

39 C. Yang, P. Chen, Y. Meng and M. Liu, Spreading Films of Anthracene-Containing Gelator Molecules at the Air/Water Interface: Nanorod and Circularly Polarized Luminescence, *Langmuir*, 2019, **35**, 2772–2779.

40 C. Yang, D. Yang, X. Zhu, Y. Meng and M. Liu, Circularly Polarized Luminescence of Langmuir–Schaefer Films of Amphiphilic Stilbene Enhanced via Interfacial Reaction with Cyclodextrins, *Langmuir*, 2020, **36**, 12366–12374.

41 K. Ma, R. Wang, Y. Rao, W. Zhao, S. Liu and T. Jiao, Langmuir–Blodgett films of two chiral perylene bisimide-based molecules: Aggregation and supramolecular chirality, *Colloids Surf., A*, 2020, **591**, 124563.

42 Y.-X. Yuan, M. Hu, M. Xue, T.-T. Zhou, Z. Zhang and Y.-S. Zheng, Circularly Polarized Luminescence and SHG Chiral Signals of Helical TPE Macrocycles, *Chin. J. Chem.*, 2021, **39**, 3353–3359.

43 P. M. L. Blok and H. P. J. M. Dekkers, Measurement of the Circular Polarization of the Luminescence of Photoselected Samples under Artifact-Free Conditions, *Appl. Spectrosc.*, 1990, **44**, 305–309.

44 G. Albano, G. Pescitelli and L. Di Bai, Reciprocal and Nonreciprocal Chiroptical Features in Thin Films of Organic Dyes, *ChemNanoMat*, 2022, **8**, e202200219.

45 L. Arrico, L. Di Bari and F. Zinna, Quantifying the Overall Efficiency of Circularly Polarized Emitters, *Chem. – Eur. J.*, 2021, **27**, 2920–2934.

46 S. P. Morcillo, D. Miguel, L. Álvarez de Cienfuegos, J. Justicia, S. Abbate, E. Castiglioni, C. Bour, M. Ribagorda, D. J. Cárdenas, J. M. Paredes, L. Crovetto, D. Choquesillo-Lazarte, A. J. Mota, M. C. Carreño, G. Longhi and J. M. Cuerva, Stapled helical o-OPE foldamers as new circularly polarized luminescence emitters based on carbophilic interactions with Ag(I)-sensitivity, *Chem. Sci.*, 2016, **7**, 5663–5670.

47 P. Reiné, J. Justicia, S. P. Morcillo, G. Mazzeo, E. García-Fernández, A. Rodríguez-Diéguez, L. Álvarez de Cienfuegos, S. Abbate, J. M. Cuerva and G. Longhi, *et al.*, Exploring potentialities and limitations of stapled o-oligo(phenylene-ethynylene)s (o-OPEs) as efficient circularly polarized luminescence emitters, *Chirality*, 2018, **30**, 43–54.

48 P. Reiné, A. G. Campaña, L. Alvarez de Cienfuegos, V. Blanco, S. Abbate, A. J. Mota, G. Longhi, D. Miguel and J. M. Cuerva, Chiral double stapled o-OPEs with intense circularly polarized luminescence, *Chem. Commun.*, 2019, **55**, 10685–10688.

49 A. M. Ortuño, P. Reiné, S. Resa, L. Álvarez de Cienfuegos, V. Blanco, J. Manuel Paredes, A. J. Mota, G. Mazzeo, S. Abbate, J. M. Ugalde, V. Mujica, G. Longhi, D. Miguel and J. M. Cuerva, *Org. Chem. Front.*, 2021, **8**, 5071–5086.

50 L. Herrer, S. Martín, A. González-Orive, D. C. Milan, A. Vezzoli, R. J. Nichols, J. L. Serrano and P. Cea, pH control of conductance in a pyrazolyl Langmuir–Blodgett monolayer, *J. Mater. Chem. C*, 2021, **9**, 2882–2889.

51 T. Schnitzer, M. D. Preuss, J. V. Basten, S. M. C. Schoenmakers, A. J. H. Spiering, G. Vantomme and E. W. Meijer, How Subtle Changes Can Make a Difference: Reproducibility in Complex Supramolecular Systems, *Angew. Chem., Int. Ed.*, 2002, **61**, e202206738.

52 M. Pedrosa, J. Maldonado-Valderrama and M. J. Gálvez-Ruiz, Interactions between curcumin and cell membrane models by Langmuir monolayers, *Colloids Surf., B*, 2022, **217**, 112636.

53 C. Roldán-Carmona, C. Rubia-Payá, M. Pérez-Morales, M. T. M. T. Martín-Romero, J. J. Giner-Casares and L. Camacho, UV-vis reflection spectroscopy under variable angle incidence at the air-liquid interface, *Phys. Chem. Chem. Phys.*, 2014, **16**, 4012–4022.

54 J. P. Coelho, M. J. Mayoral, L. Camacho, M. T. Martín-Romero, G. Tardajos, I. López-Montero, E. Sanz, D. Ávila-Brande, J. J. Giner-Casares, G. Fernández and A. Guerrero-Martínez, Mechanosensitive Gold Colloidal Membranes Mediated by Supramolecular Interfacial Self-Assembly, *J. Am. Chem. Soc.*, 2017, **139**, 1120–1128.

55 S. Paudyal, G. Sigdel, S. K. Shah, S. K. Sharma, J. D. Grubb, M. Micic, L. Caseli and R. M. Leblanc, Interfacial behavior of Proteinase K enzyme at air-saline subphase, *J. Colloid Interface Sci.*, 2022, **616**, 701–708.

56 K. Huraux, T. Narita, C. Frétigny and F. Lequeux, Solution Drying and Phase Separation Morphology of Polyacrylamide/Poly(ethylene glycol)/Water System, *Macromolecules*, 2007, **40**, 8336–8341.

57 A. N. Semenov, A. González-Pérez, M. P. Krafft and J.-F. Legrand, Theory of Surface Micelles of Semifluorinated Alkanes, *Langmuir*, 2006, **22**, 8703–8717.

58 L. de Viguerie, R. Keller, U. Jonas, R. Berger, C. G. Clark, Jr., C. O. Klein, T. Geue, K. Müllen, H.-J. Butt and D. Vlassopoulos, Effect of the Molecular Structure on the Hierarchical Self-Assembly of Semifluorinated Alkanes at the Air/Water Interface, *Langmuir*, 2011, **27**, 8776–8786.

59 R. Kaminker, X. de Hatten, M. Lahav, F. Lupo, A. Gulino, G. Evmenenko, P. Dutta, C. Browne, J. R. Nitschke and M. E. van der Boom, Assembly of Surface-Confined Homochiral Helicates: Chiral Discrimination of DOPA and Unidirectional Charge Transfer, *J. Am. Chem. Soc.*, 2013, **135**, 17052–17059.

This journal is © The Royal Society of Chemistry 2023

J. Mater. Chem. C, 2023, **11**, 2591–2599 | **2599**